Processing of multibeam water column image data for automated bubble/seep detection and repeated mapping

Peter Urban,* Kevin Köser, Jens Greinert

GEOMAR Helmholtz Centre for Ocean Research Kiel, Kiel, Germany

Abstract

Water Column Imaging Multibeam Echosounder Systems (MBES) are effective and sensitive tools for investigating free gas (bubble) release and its rise through the water column. The main advantages of MBES are the detection range and lateral coverage in the water column and at the seafloor; furthermore, they are becoming increasingly available on research vessels worldwide. However, high noise levels and systematic artefacts due to side-lobe induced signal interference degrade MBES Water Column Images (WCIs) and hampered automated bubble detection and related gas seepage investigations. We present a new technique advancing automated detection of bubble streams and moving toward a quantitative gas-release assessment. It is shown that bubble streams can be detected reliably by their spatio-temporal behavior even when they are discontinuous in WCI data. Using assumptions about the bubble rising trajectories, bubble release spots at the seafloor can be traced even if the source location is obscured by acoustic noise or unwanted acoustic targets. A map with acoustic response and source locations of bubbles being released can be produced and serves as a starting point for more detailed quantitative analyses. The efficiency of the method has been assessed at a methane seep site in the Dutch North Sea. Multiple survey lines are merged to a detailed acoustic map of the area. Processed results are in good agreement with manual investigations of the WCI data as well as ROV-based video analysis.

Active hydroacoustic systems are efficient tools for detecting and investigating free gas (bubble) seepage in lakes and oceans. Due to the strong change in acoustic impedance, gas bubbles are excellent acoustic targets that can be detected in sonar systems over a wide distance/water depth. Natural vents or seeps release erratic, cyclic or constant bubble streams that can be detected in acoustic water column data (e.g., echograms from single-beam echosounders) by their typical "flare" shape or as rising line when single bubbles/bubble clouds are ensonified. Acoustic surveys using single-beam or split-beam echosounders are nowadays a standard method for seep studies e.g., in the Black Sea (Greinert et al. 2006, 2010; Artemov et al. 2007; Nikolovska et al. 2008; Sahling et al. 2009; Römer et al. 2012), the Coal Oil Point, Santa Barbara (Hornafius et al. 1999; Leifer and Culling 2010), the North Sea (Schneider von Deimling et al. 2011), the West Spitsbergen continental margin (Westbrook et al. 2009; Fisher et al. 2011; Gentz et al.

2014; Sahling et al. 2014; Smith et al. 2014), or the Gulf of Mexico (MacDonald et al. 2002; Solomon et al. 2009; Weber et al. 2012; Rahman Talukder et al. 2013). Methods for using ship-borne scientific split-beam echosounders not just for bubble/seep detection but for gas-flux estimates are still being further advanced despite existing approaches (Artemov 2006; Artemov et al. 2007; Ostrovsky et al. 2008; Greinert et al. 2010; Muyakshin and Sauter 2010; Ostrovsky and Tęgowski 2010; Schneider von Deimling et al. 2011; Römer et al. 2012; Leblond et al. 2014; Veloso et al. 2015).

The ability to acoustically investigate large areas by single and split-beam systems is restricted by the rather small water column coverage of the main beam (width normally $< 20°$ -3 dB, often $< 10°$). Especially in shallow waters, single-beam surveys to detect and map all bubble releases in a larger area are too time-consuming to be efficient and effective. Multibeam Echosounder Systems (MBES) surpass single- and split-/beam systems in this regard as they ensonify a swath below the ship, typically covering $\sim 120°$, resulting in a significantly wider coverage per survey line.

During the last decade, water column imaging MBES are therefore used increasingly often, but data are typically still processed by manually browsing through Water Column Images (WCIs) searching for marine indications of bubble
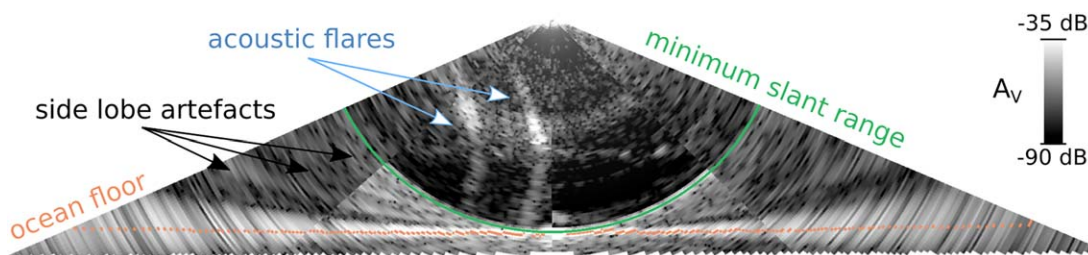
---

*Correspondence: purban@geomar.de

Fig. 1. WCI from a Kongsberg EM302 (43 m water depth). Two bubble streams are seen in this single WCI. But also bottom related side-lobes are visible which challenge the detection of bubble streams outside the minimum slant range.

release and manually localizing (picking) the source positions (Schneider von Deimling et al. 2007; Nikolovska et al. 2008; Gardner et al. 2009; Weber et al. 2012; Colbo et al. 2014). Recently more advanced manual processing strategies have been applied to increase the possibility to detect flares and create more informative seep-maps (Dupré et al. 2015). Also capabilities to create 3D images from MBES WCI have been used for manual investigations of bubble streams both with calibrated (Dupré et al. 2014) and uncalibrated MBES (Schneider von Deimling et al. 2015). Manual analyses have to ensure repeatability and reproducibility of the inherently subjective human evaluation. The need for experts and time-consuming analysis limit scalability to large datasets to such a degree that the full potential of multibeam WCI surveys for seep and bubble analyses has not yet been utilized. Manual search also limits the possibility to reprocess datasets to optimize processing parameters or to compare different processing and quantification methods as they advance. Because of this, we advocate automated machine processing and evaluation of survey data, where algorithms and processing parameters can be published and shared, ultimately facilitating a better reproducibility of dataset analysis.

In this paper, we introduce such a reproducible and effective processing routine for data filtering, bubble release identification and actual bubble vent localization at the seafloor in WCI data. We focus on investigating how well an area has been mapped to evaluate the confidence of the bubble stream detection after the survey and to support a good survey strategy ensuring complete mapping of constantly active bubble sources in an area. For this purpose, we incorporate the lateral shift of rising bubbles in the presence of water currents which proved to be useful for bubble detection (Schneider von Deimling et al. 2010; Schneider von Deimling and Papenberg 2012). The presented method allows detecting and localizing bubble release even when the actual source cannot be observed due to side-lobe artefacts or a low signal-to-noise ratio (SNR). The final result is an acoustic map related to gas release activity, including a confidence value of how well a certain spot at the seafloor has been mapped.

The method is assessed at a shallow water methane seep site in the North Sea and it is shown that the maps are consistent across different transects of the survey and are in good agreement to in situ visual observations from ROV-based video dives. We discuss limitations, the possible use for fully automated bubble stream detection and gas flux estimates in future applications.

Basic concepts

Bubble signals in single WCI images

In this work, we are interested in bubbles rising as continuous streams and the strengths of these sources (i.e., the gas flow rates) which can be empirically correlated with the acoustic response of the bubble stream (Greinert and Nützel 2004). Bubble streams are detected in WCI data through their pattern in the water column data. Gas release varies from single bubbles to mega-plumes (Leifer et al. 2006), each form of release featuring a different pattern. Here, we concentrate on constant bubble releases originating from a distinct source (bubble streams). These appear in acoustic echograms or WCIs as a flare-like shape (2D example in Fig. 1; 3D in Fig. 2a) which is why their acoustic representation is referred to as an "acoustic flare" or just "flare" (Greinert et al. 2006).

Pattern based flare detection in WCI data is challenging because the WCIs are often degraded by strong, unwanted responses, e.g., from incidental targets like shoals of fish, interferences from other acoustic systems and artefacts e.g., from the MBES beam-forming process. When strong enough, these distortions/artefacts can hide or falsify acoustic flare information and degrade data quality.

The most prominent artefacts are usually related to the strong signal return from the seafloor in interaction with the beam pattern-specific side-lobes. Such side-lobe artefacts can be seen in Fig. 1. The data quality of the WCI is strongly degraded by side-lobe interferences beyond the minimum slant range (the shortest radial distance between the sonar transducer and the seafloor). A detailed description of side-lobes and beam pattern effects in WCI data with a special focus on the seafloor as target is given in Clarke (2006).

3D WCI data processing

The 2D water column data of each ping can be translated into 3D scatter points at their real physical position and distance to each other by incorporating information on beam angles, ship motion and position, sensor offsets and sound
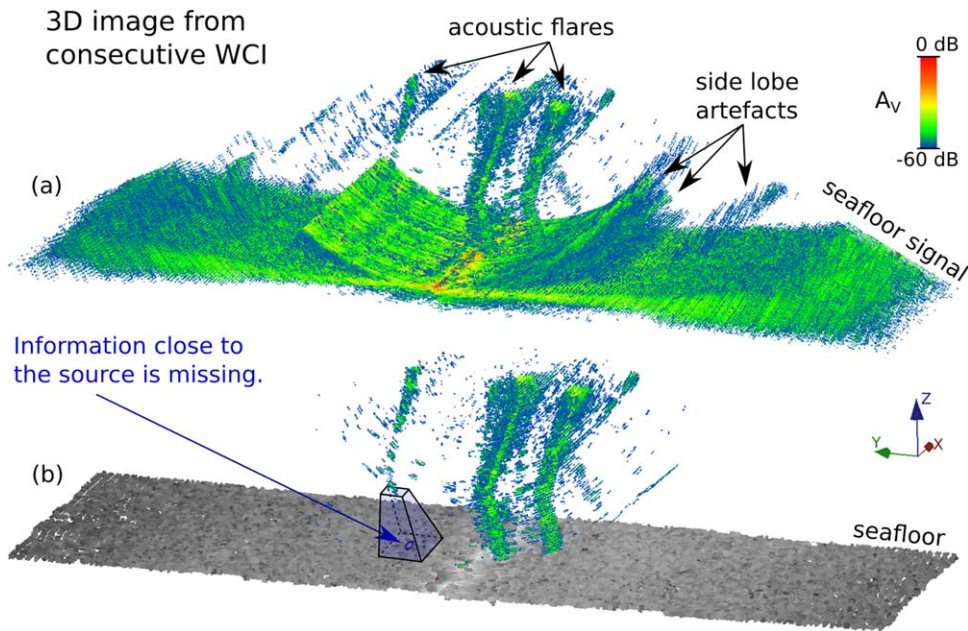
Fig. 2. (**a**) 3D data point cloud extracted from 120 consecutive WCIs. Only points depicting signals above -60 dB A_V (qualitative volume backscattering strength values (see below)) are shown. Three flares are visible in the minimum slant range. The bottom-related side-lobe effects form a half-pipe like structure along the ship's track. (**b**) All data from beyond the minimum slant range are excluded. The three acoustic flares remain as well detectable 3D point clouds. But the source location of the left flare cannot be detected since related signals were beyond the minimum slant range.

velocity profile(s) for correct ray tracing (Medwin 1998, chap. 3.3.3). The sequence of WCIs from a survey results in a detailed three-dimensional acoustic image of the water volume along the ship track. Figure 2a shows the potential of the 3D representation of WCI data. Acoustic flares appear as clouds of strong scatter points and can be described in physical terms like position and volume. However, side-lobe artefacts, acoustic interferences and noise are exported into 3D space as well and appear as strong (virtual) 3D structures. To avoid this, significant interferences, artefacts and distortions need to be identified and excluded from what can be observed during the WCI survey. Side-lobe induced structures can be excluded by accepting only those data that have been recorded inside the minimum slant range. This is illustrated in Fig. 2b where acoustic flares are well detectable but for some flares the source position cannot be observed.

Observability of flares in survey lines

To understand which parts of the water column have been investigated well enough in order to identify possible bubble streams in the 3D WCI data we define the "observable water volume." This is the complete volume of water that has been ensonified by the multibeam pings, but was not disturbed by the occurrence of unwanted targets or side lobe artefacts interfering with flare detection.

Assuming that the ping overlap of consecutive pings represented by the WCIs is high enough to detect all desired targets below the ship track (sufficiently high ping rate relative to water depth/travel time and beam angle), the

observable water volume is confined by a roof-shaped top (the outer beams) and the seafloor. By excluding data from outside the minimum slant range, the observable water volume is further limited by a cylindrical lower border (Fig. 3).

To detect bubble streams in the remaining observable water volume and identifying their release location it is necessary to connect the acoustic information about bubble streams and associate them with the respective source location.

Currents and bubble rising behavior

Varying water currents, especially in a tide-dependent open sea environment, influence the propagation path of bubble streams in the water column and thus the flares in WCI data. When identifying, describing and comparing seepage behavior it is necessary to link the acoustic information to the respective bubble release location. Treating the location as a fixed position at the seafloor makes it possible to compare bubble release strengths at different times, e.g., different tidal stages, seasons or between surveys.

Assuming that the released bubbles have a narrow bubble size distribution and neglecting small-scale turbulences, the main propagation path of a bubble stream depends on the terminal rising speed of single bubbles/bubble clouds (sum of "normal" bubble rising, possible bubble-induced upwelling forces as well as the vertical water current component) in combination with horizontal water currents, which bend the bubble propagation path. General information on bubble rise models is provided by Clift et al. (1978). Similar to Schneider von Deimling et al. (2010), we describe the lateral
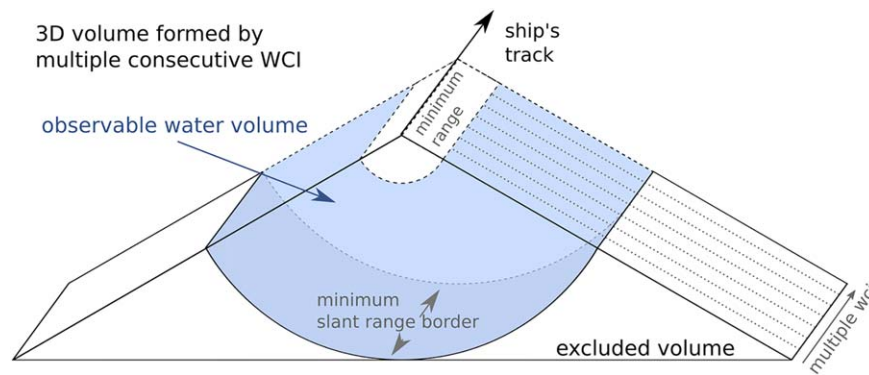
Fig. 3. Observable water volume of a multibeam survey-line segment, where the data outside the minimum slant range is excluded.
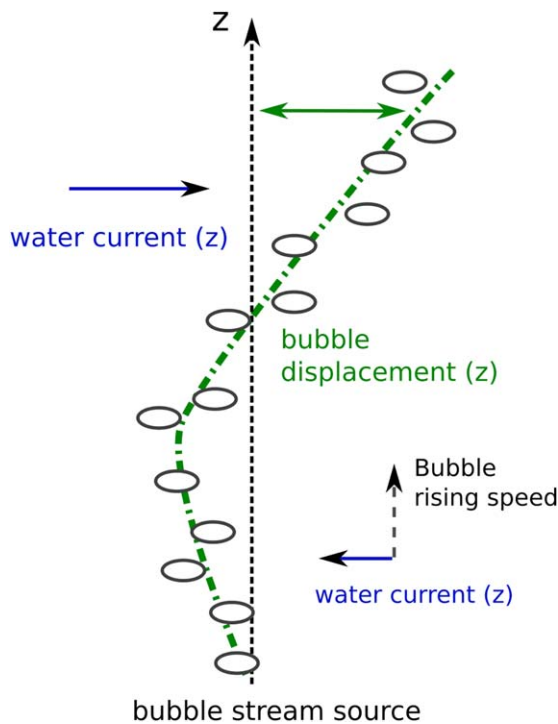

Fig. 4. Bubble stream propagation through the water column under the effect of water current. The bubble displacement is the horizontal distance between the flare propagation path in a certain depth (z) and the bubble source position. The path is determined by the vertical bubble rise velocities and the horizontal water current.

shift as depth-dependent "bubble displacement" from the seep source, which is driven by a horizontal and a vertical velocity vector (Fig. 4). With increasing vertical distance from the source, differences in the bubble-rising speed can cause the bubble stream to spread out as differently sized bubbles have different rise velocities and thus different motion vectors for the same horizontal current.

When water currents are more or less constant in a seep area and during the time of observation and when the final rise velocity of bubbles does not vary strongly between different bubble streams, the propagation path of these bubble streams will show a similar, "common" bubble displacement in the water column that can be predicted from current measurements (e.g., ADCP data).

Materials and procedures

Data acquisition and processing

This work focuses on data acquired by Water Column Imaging MBES using a Mills Cross configuration (Lurton 2010, chap. 8.3; Colbo et al. 2014) operated with standard ancillary sensors and data (GPS navigation, ship motion, sound velocity profiles). The used hull-mounted Kongsberg EM 302 (1° × 2° beam angle) is further described in the "Assessment" section.

The software FMMidwater from QPS (FMMidwater 2014) has been used to gain an initial overview of the dataset while assessing our method and to convert the raw multibeam data into the Fledermaus Generic Water Column format (.gwc) (IVS 3D, Inc 2012). These files were further processed with a set of custom-developed tools.*

Similar to MBES seafloor mapping surveys, usually multiple WCI survey lines are necessary to completely cover a seepage area. To ensure complete mapping of all bubble streams the WCI survey is planned as a set of parallel lines close enough to ensure that the observable water volume overlaps rather than only the detected bottom. The survey speed of the vessel should be as low as possible to prevent gaps between consecutive pings.

Calculating absolute or relative volume backscattering strength

An important first step in processing raw WCI data is to calculate the correct range-dependent volume backscattering values. In this paper, the volume backscattering strength S_V is used as an indicator for the sum of target cross sections

---

*For more information see: http://www.geomar.de/~deepsea-monitoring-e.

per unit volume. The echo level (EL) received for volume scatterers can be approximated from the sonar equations (Urick 1996):

$$EL = SL - TL + S_V + 10 \log (V) \tag{1}$$

Where SL is the source level, TL is the transmission loss that depends on the range from the transducer (r) and the logarithmic attenuation coefficient (α):

$$TL = 40 \log (r) + 2\alpha r \tag{2}$$

S_V is the volume backscattering strength and V is the sampling volume which can be approximated from the sampling time (t) the speed of sound (c) and the effective beam solid angle (ψ):

$$V \approx \frac{ct}{2} \psi r^2 \tag{3}$$

The relation between received echo levels (EL) and the raw WCI sampling amplitudes A_{WCI} depends on several factors including frequency, bandwidth, digital-to-analog-converter sensitivity, receive beam pattern and is also subject to transducer aging processes. This relation is described here by a constant calibration factor (CF) and must be obtained by system calibration. Additionally, most MBES apply a time-varying gain (TVG) to the received acoustic intensities, which accounts for spreading and acoustic absorption in such a way that the analog-digital-converters can work at ideal conditions for the entire signal propagation path/time. Because the TVG is not constant, it must be considered separately from CF and A_{WCI} relates to EL in the following way:

$$A_{WCI} = EL + TVG + CF \tag{4}$$

S_V can then be calculated from the WCI sampling amplitudes (A_{WCI}) by:

$$S_V = A_{WCI} - (TVG - 20 \log (r) - 2\alpha r) - 10 \log \left(\frac{ct}{2}\psi\right) - SL - CF \tag{5}$$

During the assessment of the proposed method the Kongsberg EM302 is used for which the following TVG function is specified:

$$TVG = X \log_{10} (r) + 2\alpha r + OFS + C \tag{6}$$

Herein X is the TVG spreading loss factor which was set to 30 during the survey. The offset calibration factor C allows manufacturer system calibration. OFS is a system specific gain offset that compensates for transmit source level, pulse length, receiver bandwidth, receiver sensitivity and the receive- and transmit-beam pattern along and across track corrected for roll and pitch (Kongsberg support, pers. comm.). The unknown constant factors of the previous equations can be summed up to a single factor (C_{Sv}) which could be obtained by MBES calibration:

$$C_{Sv} = OFS + C + CF + SL + 10 \log (\psi) \tag{7}$$

The calibration of MBES is problematic as tank experiments are usually necessary (Foote et al. 2005; Perrot et al. 2014), which are difficult to carry out for already installed, hull-mounted MBES. In this case, the calculation of absolute S_V values is not possible and only qualitative volume backscattering strength values (A_V) can be calculated which differs from S_V by the constant factor C_{Sv} as follows:

$$S_V = A_V - C_{Sv} \tag{8}$$

The qualitative volume backscattering strength A_V can then be calculated using the following formula (compare also Gurshin et al., 2009):

$$A_V = A_{WCI} - (X - 20) \log (r) - 10 \log \left(\frac{ct}{2}\right) \tag{9}$$

It should be noted that for an uncalibrated system, calibration differences between beams may occur which would cause further uncertainties. As the values for backscattering strength in WCI data from different systems/manufacturers are calculated differently (e.g., varying TVG functions) the calculation of S_V or A_V may vary between systems.

While throughout this work A_V is expressed in dB, it is important to note that all arithmetic mean computations have been carried out in linear domain by the following equation:

$$\bar{A}_V = 10 \log \left(\frac{1}{N} \sum_{n=1}^{N} 10^{\left(\frac{A_{V,n}}{10}\right)}\right) \tag{10}$$

Masking and excluding static acoustic distortions

We propose two different methods for excluding static acoustic distortions. As mentioned in the basic concepts, a simple and effective way of excluding side-lobe artefacts is the exclusion of all data outside the minimum slant range usually providing a clean and reliable dataset under varying environmental conditions (see Fig. 2). The minimum slant range can be detected in MBES WCI using the system integrated bottom detection. The minimum slant range corresponds to the range of the earliest detected bottom return value (Fig. 5b).

However, since side-lobe distortions are systematic they can be detected and masked selectively under certain circumstances: For roll and pitch compensated MBES in a flat seafloor area, all related side-lobe artefacts appear in a similar way during the entire survey. After applying heave compensation, the background A_V level (B_V), which includes the systematic side-lobe distortions, can be estimated by stacking consecutive WCIs and calculating the median signal level for each acoustic sample in the beams. Areas in WCIs that exceed a threshold in the stacked median image can then be marked as not observable (Fig. 5).
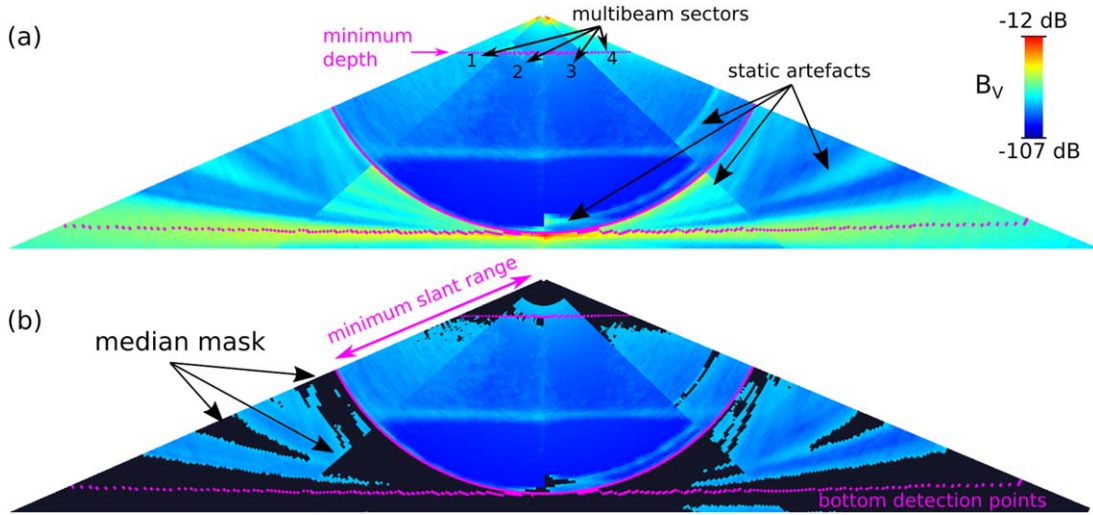
Fig. 5. (**a**) The background A_V level (B_V) of the Kongsberg EM302 swath over a horizontal seafloor in ca. 42 m water depths estimated as median over 1000 pings. Because of the horizontal seafloor, the seafloor-related side-lobe artefacts occur as constant background levels. (**b**) Mask created from the median signal level (with B_V threshold of -87 dB). Shown in this image is also the minimum slant range which was detected from the MBES internal bottom detection points.

The median has a breakdown point of 50% (cf. to Hampel 1971). We therefore suggest that the median filter length (the number of consecutive pings/WCIs used to create the median image) should be three times the number of pings that ensonified the widest detected flare to avoid the influence of bubble-related signals on the median stack image.

Bubble displacement from interactively extracted template flares

While water currents can be measured by ADCP, in the following we describe a methodology for determining the bubble displacement if no ADCP information is available. The bubble displacement can be extracted from an interactively detected strong flare acting as a "template" (Fig. 6). A "good" flare features strong signal returns that clearly separate the flare from the background signal level, interferences and other flares; it depicts bubble related information for all depth levels that are investigated and the bubble source position can be clearly defined.

To calculate the bubble displacement from such a flare, the corresponding data points are extracted into 3D space. The amount of unwanted noise related data points is reduced by adjusting the signal threshold to a maximum level. Additionally, strong artefacts and close-by flares should be deleted manually. The 3D space is divided into a discrete number of vertical slices where every slice represents a discrete depth range ($\tilde{z}$) in the water column. The 2D bubble displacement vector $\vec{b}_{\tilde{z}}$ for each $\tilde{z}$ is then calculated similarly to a center of mass, but with respect to the volume backscattering strength values $A_{V;i}$ for all N_d points inside discrete depth ranges:

$$\vec{b}_{\tilde{z}} = \frac{1}{\sum_i A_{V;i}} \sum_{i=1}^{N_d} A_{V;i} \left(\vec{r}_i - \vec{R}_{\tilde{z}_{source}} \right) \qquad (11)$$

Here, $\vec{r}_i$ are the horizontal 2D coordinates of the respective point and $\vec{R}_{\tilde{z}_{source}}$ is the exact horizontal 2D source location of the template flare. The ideal template flare characteristics are usually found for a bubble source directly beneath the ship track. When no template flare can be found where the source location is observable, the exact geo-referenced position of all flares cannot be extracted. But even then it is possible to use the flare shape for differentiating them from other targets or noise. In case the flare information is only obscured very close to the seafloor, the source location can be estimated from extrapolating the line between the deepest two $\vec{b}_{\tilde{z}}$; however, this would also mean uncertainty regarding the precision of the source location.

Mapping flares in the observable water volume

With the approximate model for bubble displacement, every data point in the observable water volume can be assigned to exactly one possible source location at the seafloor, even when the water volume close to the respective seafloor location cannot be observed. For a simplified analysis, we shift the entire observable water volume (including all borders of observability) inverse to the bubble displacement of the temporally and spatially closest flare template. This transformation of the 3D volume causes all acoustic flares following the bubble rise model to form straight vertical pillars above their source position (Fig. 7). We therefore refer to this process as rectification of the observable water volume. All further processing is then applied to a 3D voxel grid in which each voxel inside the rectified observable water
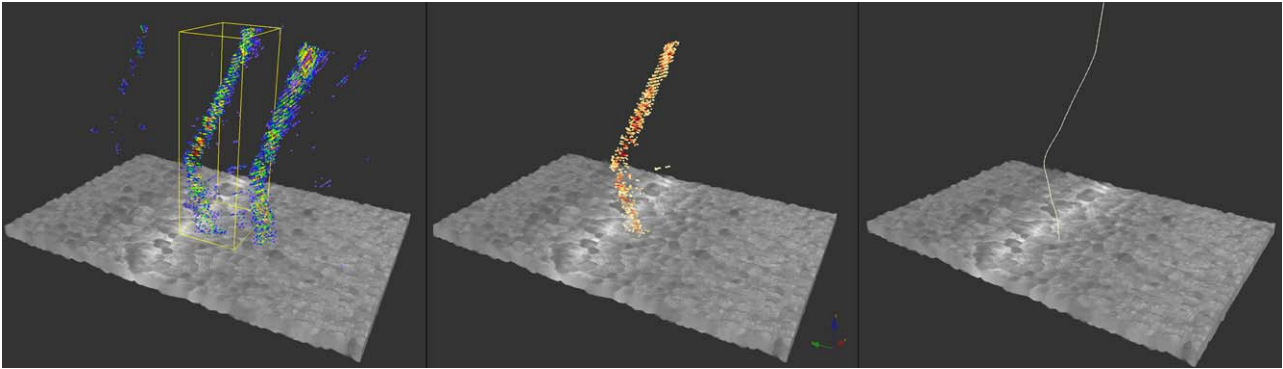
Fig. 6. Example for extracting a flare template. First, a model flare is interactively separated from the surrounding signals. A high threshold decreases the influence of low amplitude noise. The spine of the flare (which is used as flare template) is constructed by calculating the weight point of the remaining scatter points at a discrete number of heights.

volume contains the mean volume backscattering strength of all N_v acoustic samples that are inside the respective voxel (average grouped voxel A_V (A_{vox})):

$$A_{vox} = 10 \, \log\left(\frac{1}{N_v} \sum_{n=1}^{N_v} 10^{\left(\frac{A_{V;n}}{10}\right)}\right) \qquad (12)$$

All other voxels outside the observable water volume are marked as "not observable." The voxel size determines the resolution of the 3D analysis and should match the physical distance of the acoustic samples in such a way that all voxels inside the observable water volume can be filled with data.

When the acoustic signals above a location continuously exceed the acoustic background level, this indicates the source location of a bubble stream, i.e., the vertical average over all A_{vox} values in the water column ($\bar{A}_{|vox}$) above a seafloor location can be used as a value for "flare indication." To increase robustness against signal outliers (e.g., strong responses from isolated fish or artefacts), the median value ($\tilde{A}_{|vox}$) rather than the arithmetic mean is used as flare indication value. The resulting flare indication values are finally written into a geo-referenced acoustic flare map of the seafloor.

The rectified observable water volume above a seafloor position corresponds to how much of a hypothetical flare would be observable. The greater this volume the better flares can be separated from smaller targets or artefacts that would only occur in a small part of the propagation path. The number of vertically observable voxels ($N_{|vox}$) associated to a source location (after rectification) is therefore used as "confidence value" for the acoustic flare map. A minimum confidence value threshold is used to determine whether a seafloor location has been mapped well enough to make statements about the (non-)existence of flares, i.e., whether the available data allow for a confident flare detection.

Merging survey lines to one joint acoustic flare map

For providing acoustic maps that allow interpreting bubble release intensity in an investigated area, we use a depth layer of a certain thickness above the seafloor in the rectified observable water volume (Fig. 8). For a shallow water scenario, the depth of this layer can be defined by the maximal possible horizontal extent inside the minimum slant range. For all grid positions where the flare indication value ($\tilde{A}_{|vox}$) exceeds a chosen flare detection threshold, the N_z grouped voxel averages (A_{vox}) inside this layer are vertically averaged to determine the "relative flare intensity" value:

$$\underset{zmin}{\overset{zmax}{}} \bar{A}_{|vox} = 10 \, \log\left(\frac{1}{N_z} \sum_{n=1}^{N_z} 10^{\left(\frac{A_{vox;n}}{10}\right)}\right) \qquad (13)$$

Where zmin and zmax indicate the depth extent of the layer.

A joint acoustic flare map from several survey lines is created by merging the WCI survey lines after they have been processed individually. As discussed earlier, individual backscattering volume strength values of individual lines are not well comparable as the flare shape changes when the related bubble stream has been investigated at different range/angle from the transducer. Merging lines by averaging the acoustic values is therefore not reasonable. When two lines cover the same location the data from the line with the better confidence value ($N_{|vox}$) is taken to ensure mapping quality and data consistency.

Acoustic flare maps must be interpreted by considering that flares spread out over multiple map grid cells because of beam width, side-lobe effects and bubble spreading. Weaker single flares appear as small points at their source position. The stronger the return signal of a flare location, the larger the point appears as it is also observed by neighboring beams and pings/WCIs. Where the gas sources are too dense, the return signals from several bubble streams merge to a flare

(a) Bubble streams in the observable water volume.
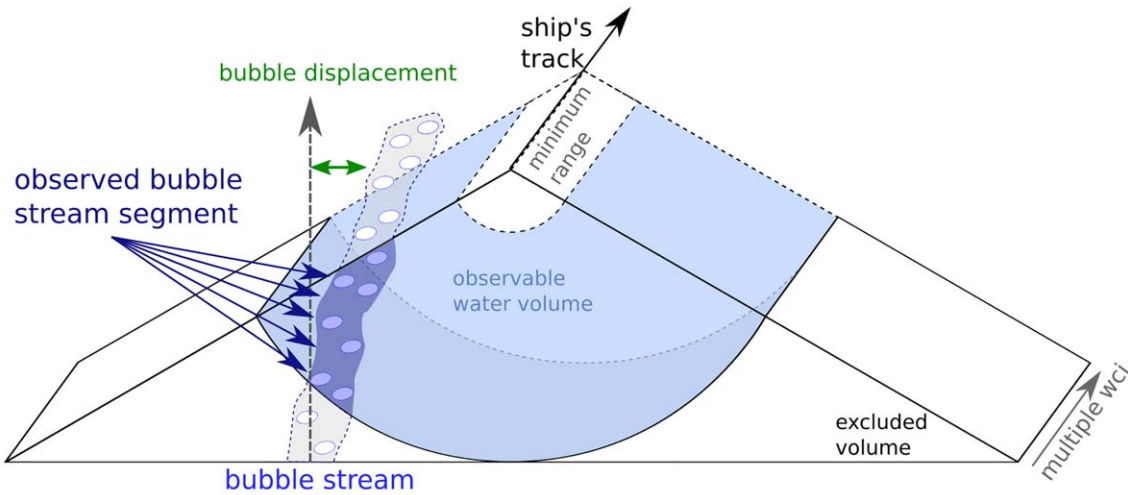
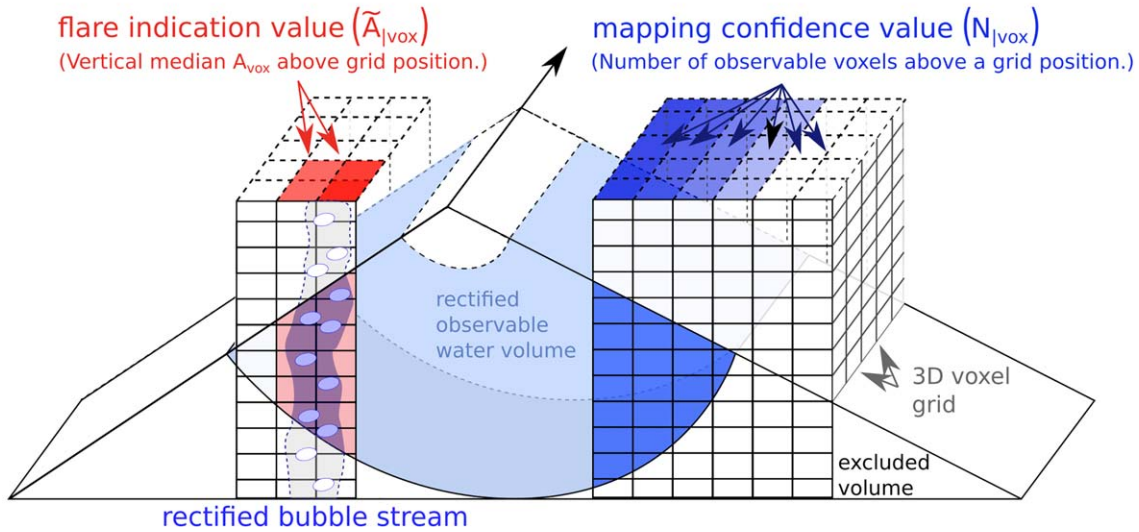## (b) Bubble stream in the rectified observable water volume.

Fig. 7. (**a**) The observable water volume is investigated in a 3D voxel grid. A part of the bubble stream is inside the observable water volume, but the source position is obscured. (**b**) The observable water volume has been deformed by the rectification with a flare template (rectified observable water volume). The observable part of the bubble stream aligns straight above its source position. The median signal level above a seafloor location is used as indication value for a flare emerging from this position. The number of voxels above a seafloor location indicates how much of such a flare would have been seen in a WCI survey. It is used as mapping confidence value.
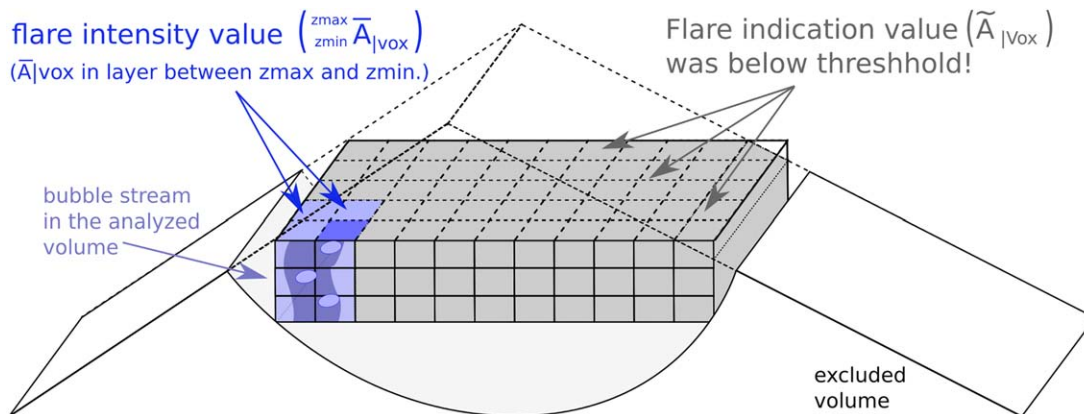
Fig. 8. The volume used for quantitative analyses after false targets have been excluded by a seepage detection mask equals the observable water volume with a minimum and maximum depth limit applied.

area rather than single spots at the seafloor. This is shown in the following assessment.

Assessment

Study area and dataset

The dataset used for the assessment was acquired during a cruise by the Royal Netherlands Institute for Sea Research (NIOZ) on RV *Pelagia* in September 2013 (64PE354). The investigated area is located in the Netherlands' EEZ in North Sea Block B13 south of the Dogger Bank. Seepage in this block was described by Schroot et al. (2005). A 2D seismic line revealed a Plio-Pleistocene gas field ca. 600 m below the seafloor. Using a single-beam echosounder, two flares were found indicating gas release into the water column. The site has also been revisited by Mau et al. (2015)

who investigated the dissolved methane distribution in the area, but also manually detected flares in EM710 multibeam data.

For this assessment, we used a part of the acquired dataset, highlighted in Fig. 9. The bathymetric map shows a nearly featureless flat seafloor at 43–45 m water depth. The water column survey lines were planned as straight E-W running lines with 50% line overlap at the seafloor. The mean speed over ground was about 4.5 knots and the average ping interval 205 ms. The along-track distance between two pings was between 0.41 m and 0.52 m.

The EM302 on board RV *Pelagia* is a 30 kHz Mills Cross MBES with a nominal depth range from 10 m to 7000 m, a transmit swath width of up to 150°, a beam width of 1° × 2° and up to 288 beams. It has roll, pitch and yaw compensation using multiple sectors with different center frequen-
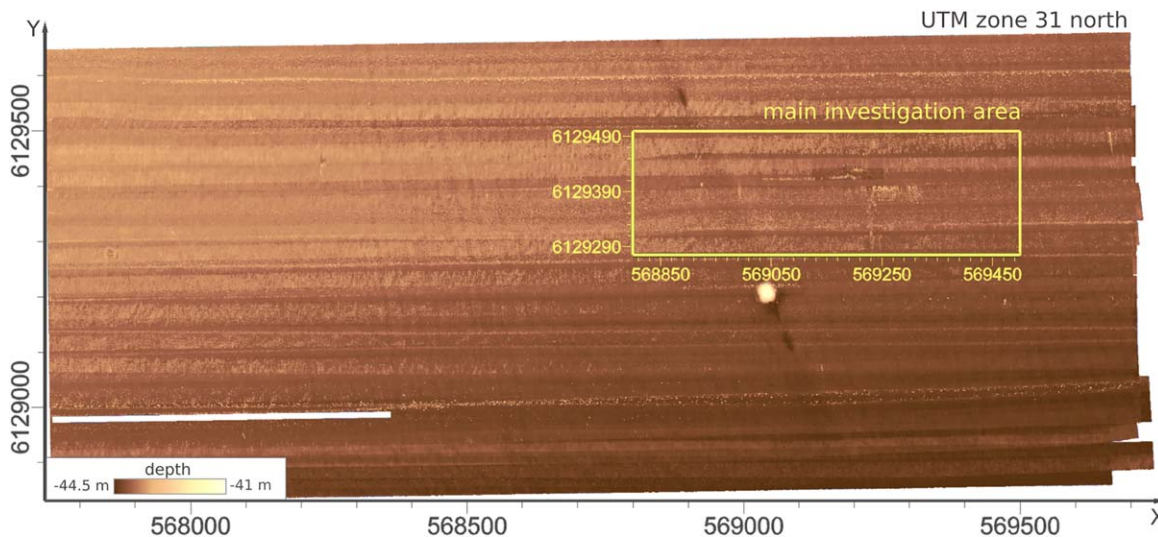

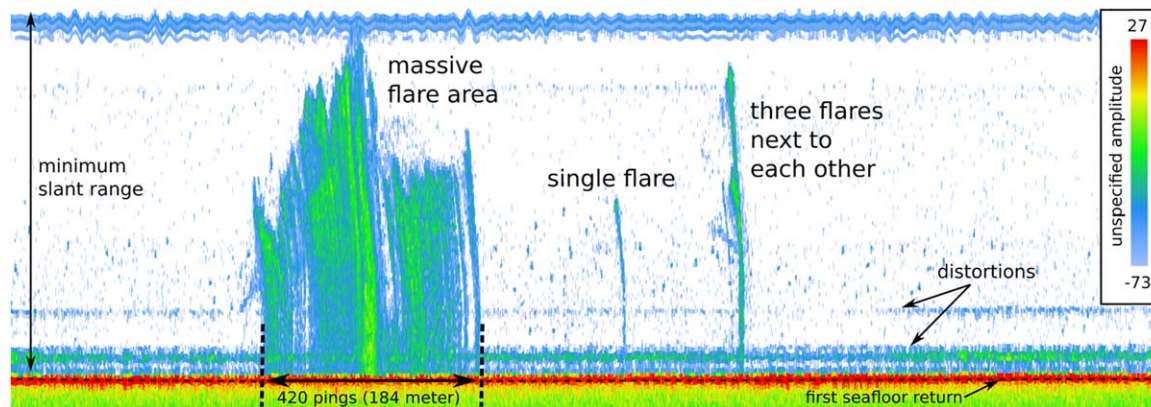**Fig. 9.** Bathymetric map of the area.

Fig. 10. FMMidwater stacked view of one survey line. Unspecified amplitude corresponds to the raw unprocessed amplitude values as given by FMMidwater. The red line corresponds with the first return from the seafloor. Several flare-shaped targets can be detected instantly.
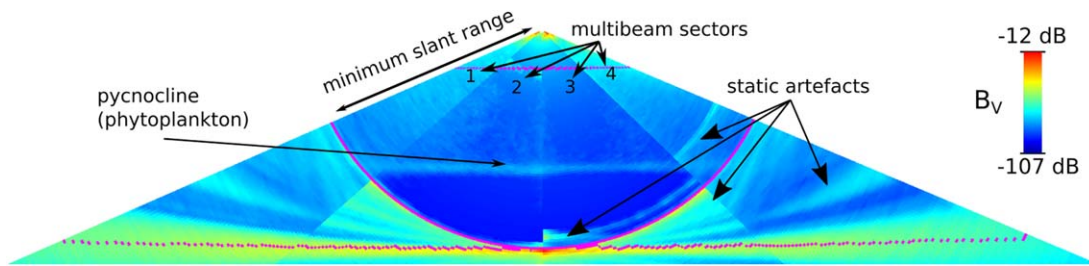
Fig. 11. Background signal level of the Kongsberg EM302 swath over a horizontal seafloor in ca. 42 m water depth estimated as median over 1000 pings. The Kongsberg EM302 uses at least four different sectors for yaw and pitch compensation. These sectors use slightly different base frequencies and a ping delay toward each other. This delay causes side-lobe artefacts to occur in the sectors 3 and 4 even inside the minimum slant range.
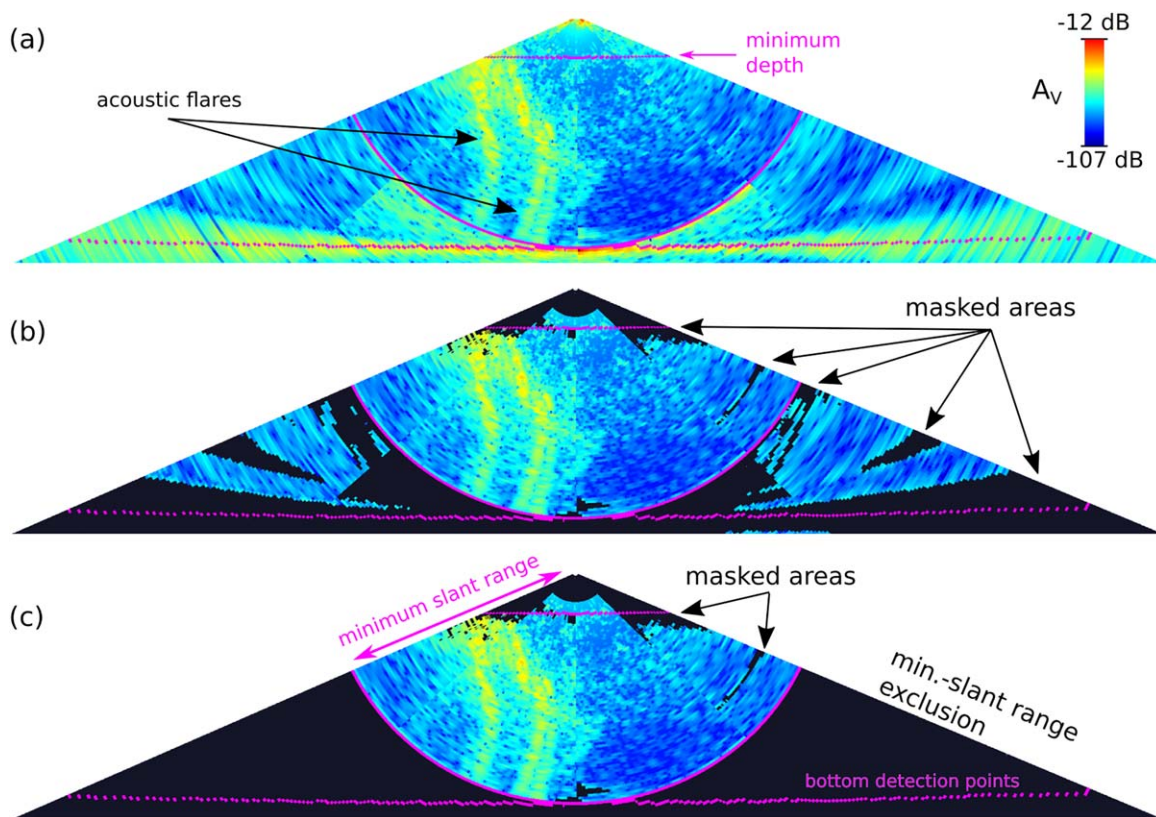

Fig. 12. Masking static artefacts in the swath image. In purple are shown: the minimum depth (12 m), the MBES system bottom detection points and the minimum slant range which was determined from these points. (**a**) Raw swath image with two flares visible. (**b**) Composite image resulting from applying a mask(shown in black) to the swath image. The mask was generated from the median signal level (Fig. 11) with a maximum B_V threshold of -87 dB (**c**) Additionally to median masking all data from beyond the minimum slant range where excluded (will be used for comparison).

cies and variable tilt angles. During the survey, the system was operated in shallow water mode with equi-angular beam spacing, and a swath width of 120°. The dual swath mode was deactivated (refer also to section "Comments and recommendations" section). A first inspection of the dataset in FMMidwater revealed multiple flares spread over the investigation area with one dominant flare area close to the position of one of the flares described by Schroot et al. (Fig. 9).

The stacked data view in FMMidwater showed that the main seepage area extends over 420 pings or 185 m (Fig. 10). During the cruise bubbles were also observed visually at the sea-surface.

Survey specific WCI processing

Masking static acoustic distortions

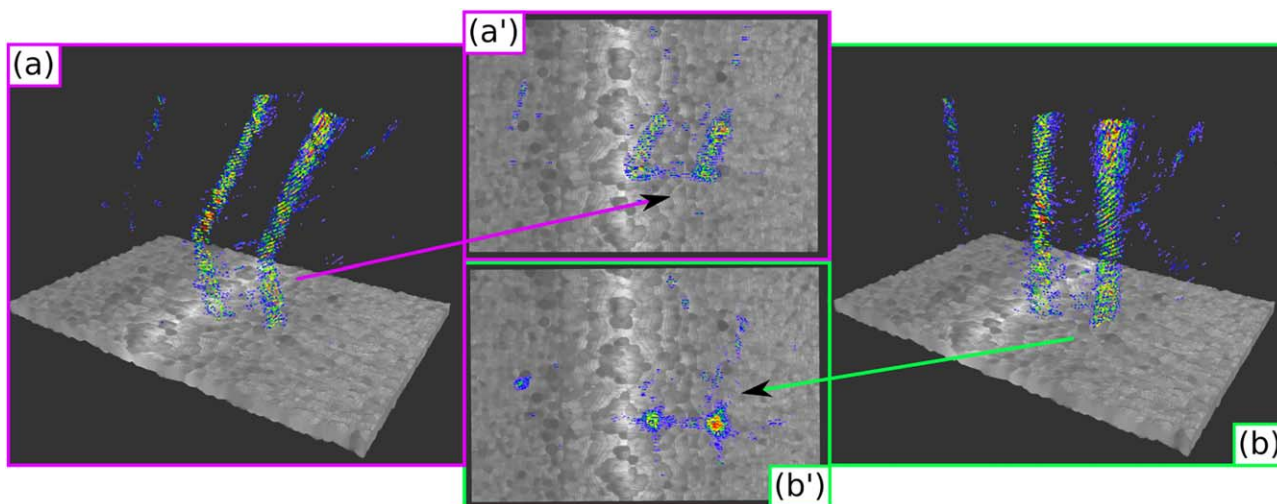Since the system electronically compensated roll and pitch, we could apply the median stacking method to

Fig. 13. Effects of the bubble displacement rectification: (**a**) 3D representation of current shifted flares. The bottom is colored gray. (**a′**) Top-view of (**a**) (**b**) Water column samples have been shifted according to the bubble displacement that has been calculated from the middle flare. (**b′**) Top-view of (**b**). It can be seen that applying the correct bubble displacement causes the scatter points of the flares to form straight pillars above the likely source position.
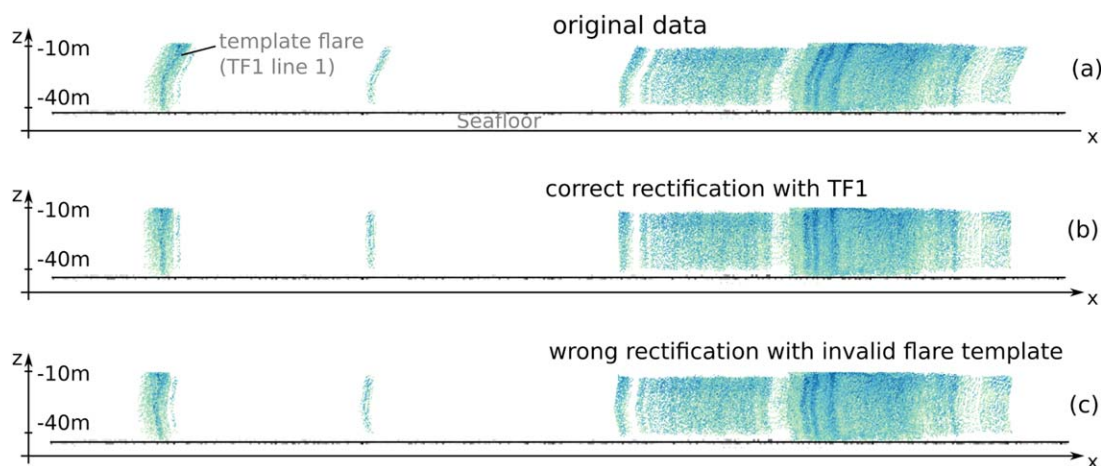

Fig. 14. Rectification with manually extracted flare templates. (**a**) Flares in the observable water volume. (**b**) Flares rectified with the bubble displacement from template flare TF. (**c**) Flares "rectified" with a template flare extracted from a survey line recorded 45 min later. The bubble displacement template was not valid anymore and the rectification did not work properly.

detect the occurrence of static artefacts (Fig. 11). The number of consecutive WCIs used to create the median image was chosen to be three times the size of the largest flare area (here 1200 pings; compare: Fig. 10). The resulting median swath image (Fig. 11) revealed systematic degradations from side-lobe artefacts also inside the minimum slant range, which can be explained by the ping delay of the different sectors. The outer sectors have a slightly higher noise level. The horizontal line inside the minimum slant range was caused by phytoplankton accumulating above a strong pycnocline (see also Brussaard 2013).

The resulting median swath image (B_V) (Fig. 11) revealed systematic degradations from side-lobe artefacts also inside the minimum slant range, which can be explained by the ping delay of the different sectors. The outer sectors have a slightly higher noise level. The horizontal line inside the minimum slant range was caused by phytoplankton accumulating above a strong pycnocline (see also Brussaard 2013).

For the median signal-based mask a threshold (B_V) of -87 dB was chosen (Fig. 12b), i.e., locations in B_V image with higher values are masked out The minimum distance from the sea surface was set to 12 m to avoid influence
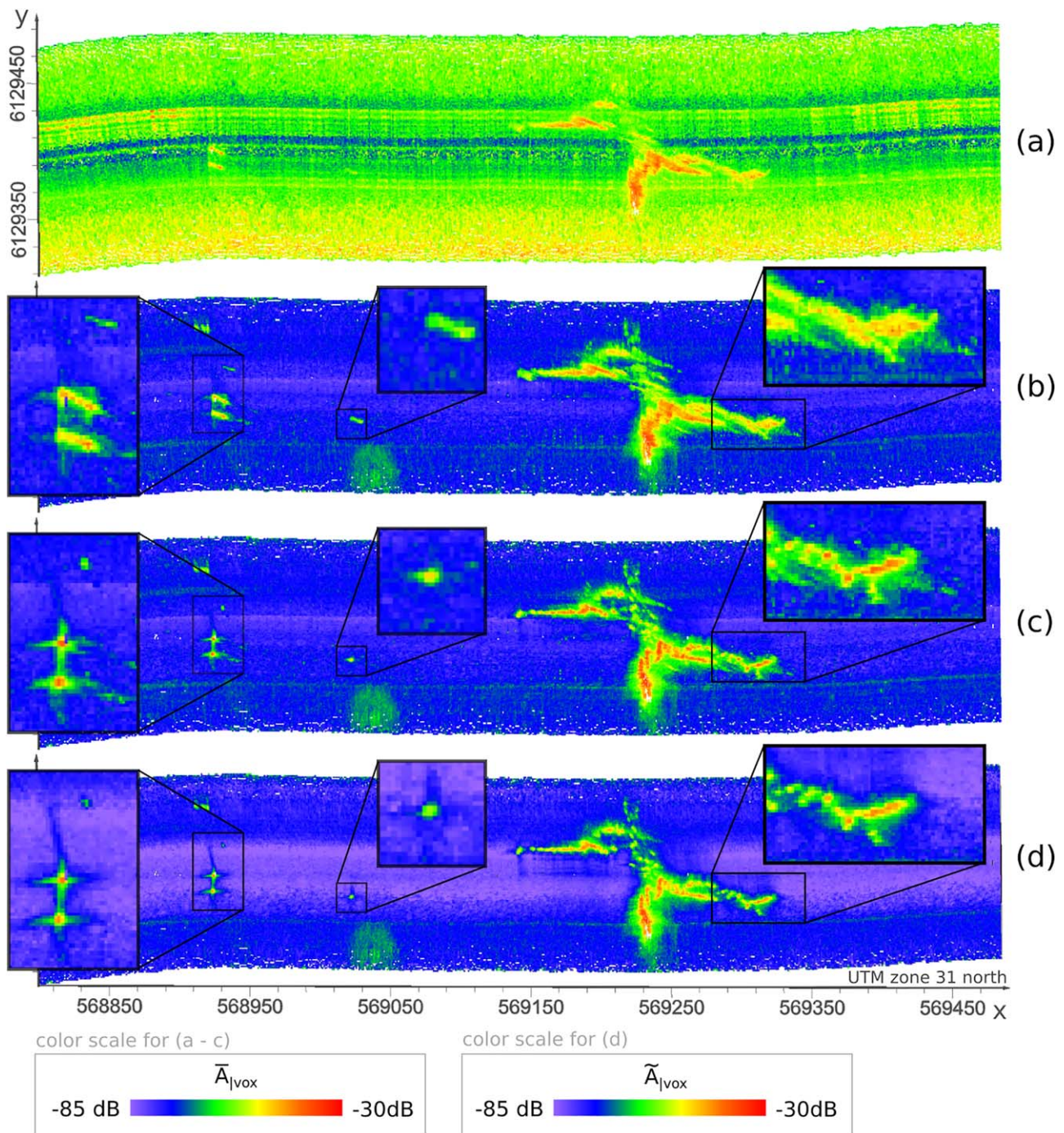
Fig. 15. Effects of processing and masking shown at the resulting flare indication map for one survey line. (**a**) Average signal strength of the whole water column above the seafloor $\bar{A}_{|vox}$ when all WCI information is used without any exclusion. (**b**) A median mask (Fig. 12) was applied to the WCI before exporting the information into 3D. Flares now become visible structures in the vertically averaged image. (**c**) Vertically averaged image after the rectification process. Flare structures gather at their likely source position. (**d**) The vertical median ($\tilde{A}_{|vox}$) rather than the arithmetic mean is used. The effect of high intensity interferences decreases which indicates that this value is best suited as "flare indication value."

from the ship's wake. The minimum slant range was determined from the EM302 bottom detection algorithm by choosing the closest bottom detection sample that occurred. Alternatively to using the median masking method, a second dataset was prepared where all points from beyond the minimum slant range were excluded to compare the differences in the observable water mass (Fig. 12c).
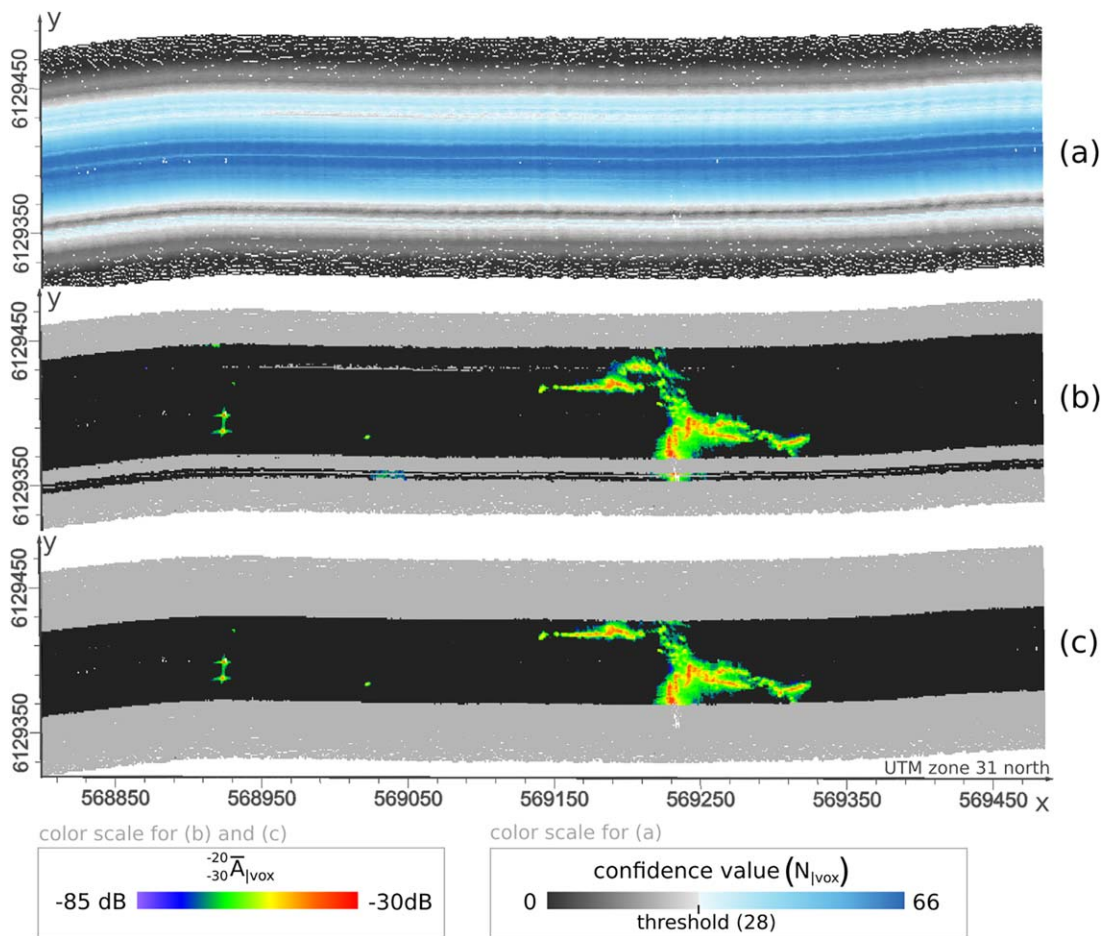
Fig. 16. Flare detection filter. (**a**) The mapping confidence (in observable voxels above a seafloor location). Points below the threshold are shown in gray. (**b**) Average A_{vox} in a depth layer between -20 m and -30 m water depth $_{-30}^{-20}\bar{A}_{|vox}$ (relative flare intensity compare Fig. 8). The map data were filtered with a minimum confidence value (28 voxels = 14 m) {excluded area is shown in light gray color} and a minimum flare indication value (-70 dB applied to Fig. 15d) {filtered area is shown in dark gray color}. (**c**) Additionally to the median mask, all WCI information from beyond the minimum slant range have been excluded (refer to Fig. 12) before calculating $_{-30}^{-20}\bar{A}_{|vox}$. This further limits the observed seafloor area.

Determining 3D voxel resolution

To avoid empty voxels in the observable water volume, the voxel size was matched to the worst-case estimates for the distance of consecutive pings/adjacent acoustic WCI samples. The maximum horizontal distance between two samples was approximated for 256 beams, with equiangular beam spacing over a 120° swath opening angle at 43 m water depth to be less than 0.5 m. The along-track distance between two pings was up to 0.52 m and considered the limiting factor for horizontal voxel size. Since the along-track distance between samples varies depending on yaw and pitch, we chose the horizontal voxel size to be 1 m by 1 m. The greatest vertical distance between two neighboring samples is dictated by the sample spacing (0.46 m) of the nadir beam samples. The worst case vertical distance between the 3D samples does not increase with variations in heave, yaw, roll or pitch and therefore the vertical voxel size was set to 0.5 m to reach the maximum vertical voxel grid resolution for the water volume analyses.

Rectification using flare templates

For the rectification of the observable water volume, flare templates were extracted manually. When the extracted bubble displacement is applied to other flares by shifting the observable water volume accordingly, it can be seen that flares around the model flare form straight pillars above their source position (Fig. 13).

One template flare per line was extracted and applied for rectification. Sailing one survey line took approximately 15 min. The applicability of the extracted flare templates to a survey line is visualized in Fig. 14.

Mapping the seepage area

In this section, the effects of each processing step are shown step by step for one survey line example. As a
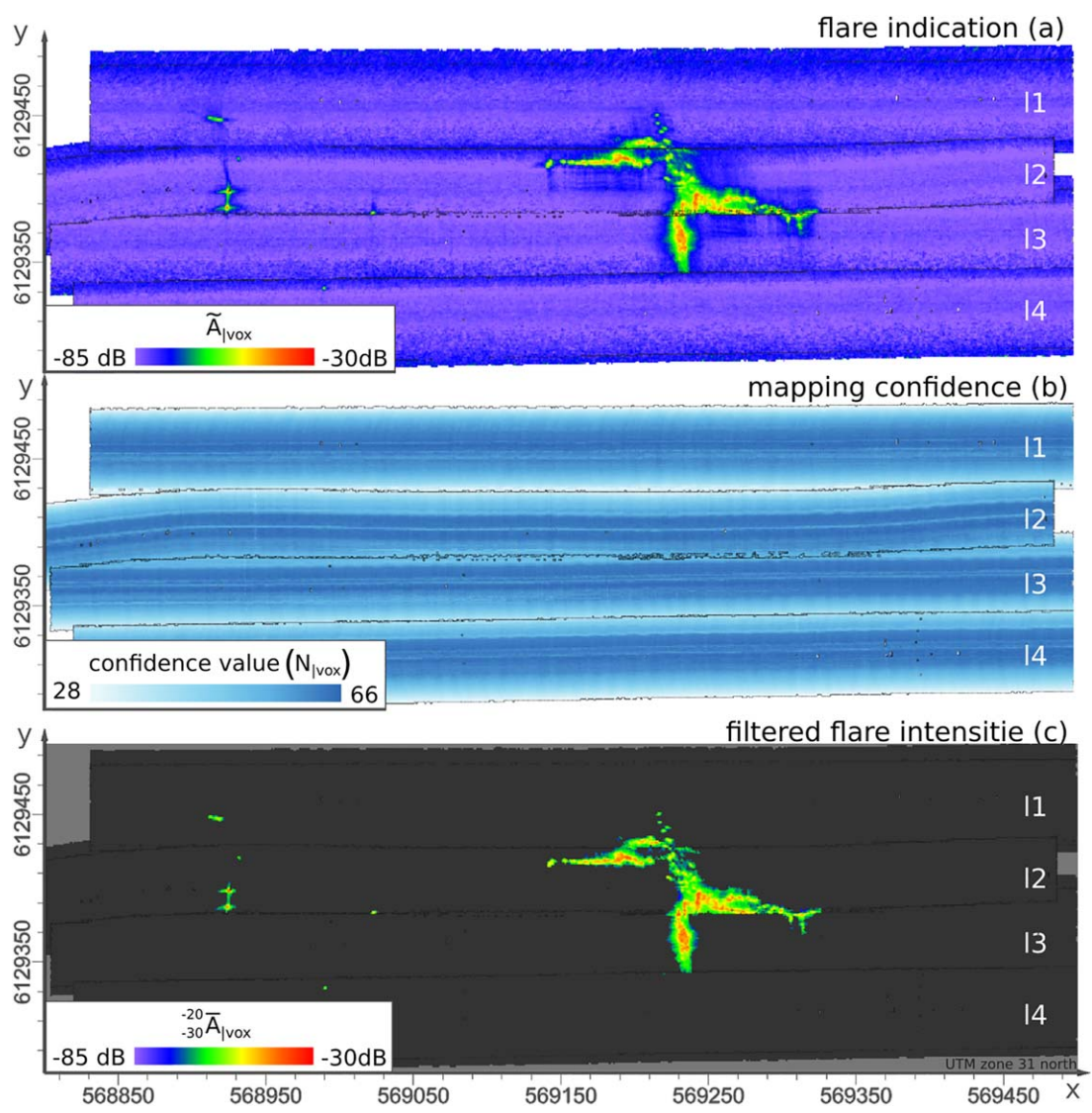
Fig. 17. Acoustic flare map created by merging four survey lines (l1, l2, l3, and l4 are framed in black) which were processed as described in the previous section. (**a**) Flare indication value (processed similar to Fig. 15d). (**b**) Mapping confidence of the area (processed similar to Fig. 16a). (**c**) Relative flare intensity values (depth layer between −20 m and −30 m; processed similar to Fig. 16c).
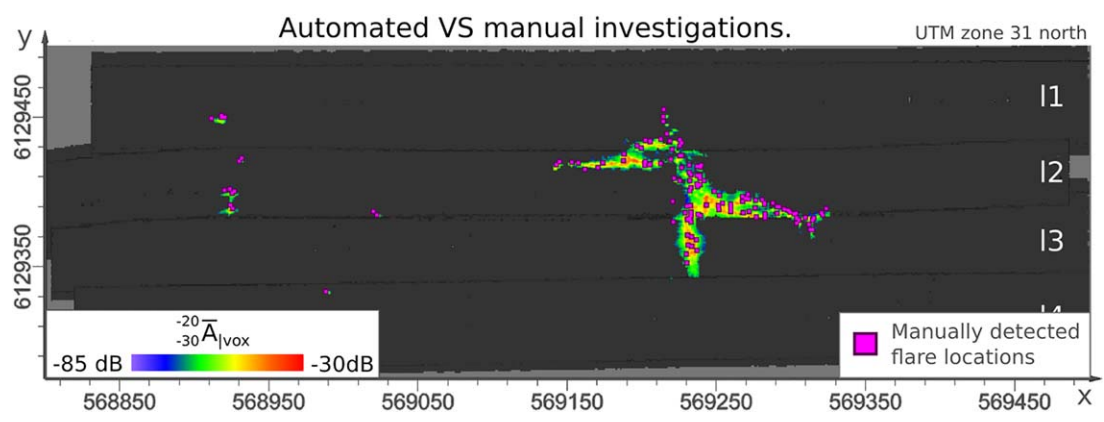

Fig. 18. (**a**) Manual flare detection in FMMidwater vs. acoustic flare map.

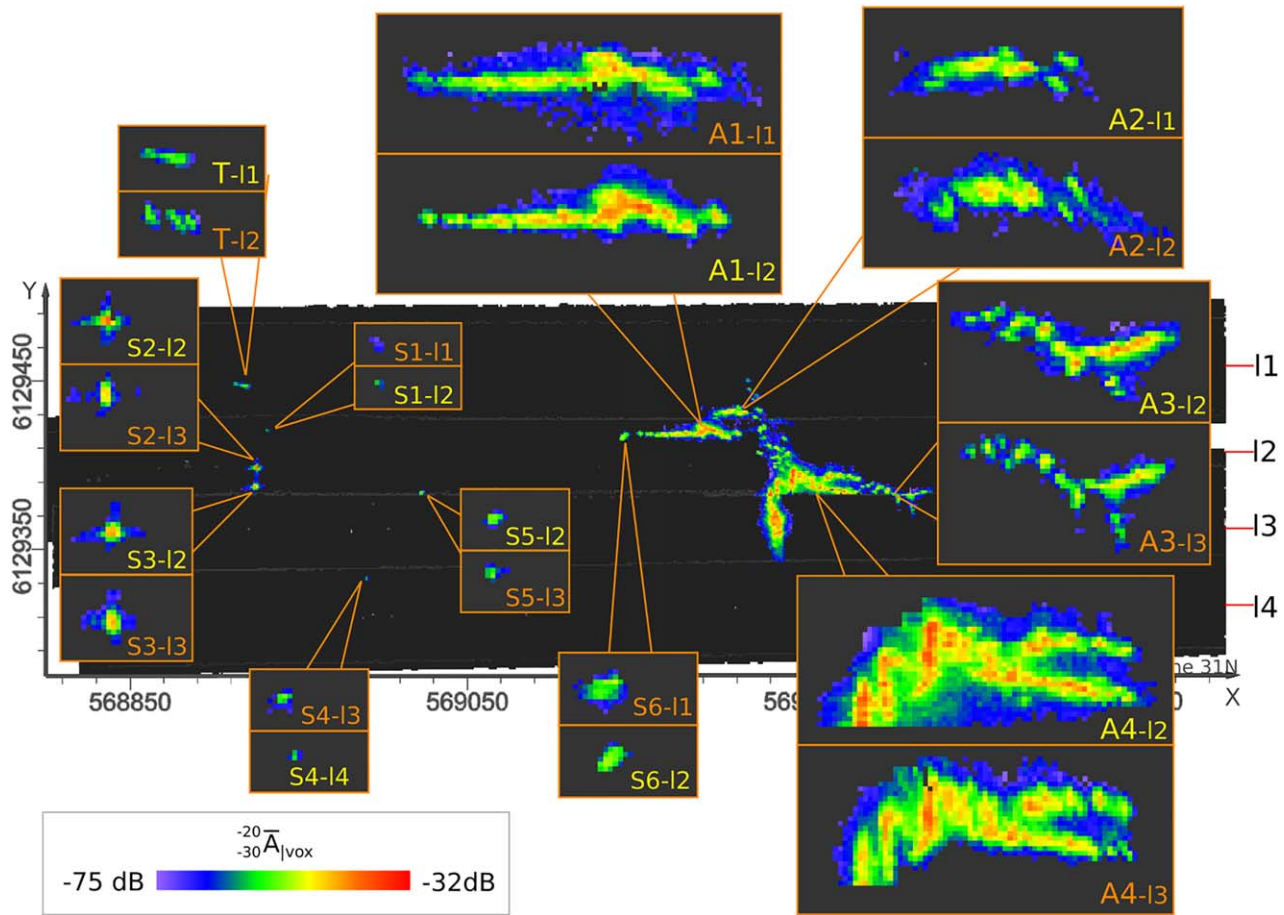**Fig. 19.** Relative flare intensity $-30-20A|vox$ map of investigated area. Flares that were observed in two lines are magnified and compared (see Table 1). **S** marks single flares; **A** marks a flare area, while **T** marks a flare that is neither a distinct single flare nor an area of flares. **I** is the line number (from north to south). Read: **S3-I2 -> single flare 3** as seen in **line 2**. The flares/flare areas from the line that appear on the final merged map are marked yellow (otherwise orange). Dominant in the area are the single flares S2 and S3 and the massive flare area (A1–A4) further the east.

baseline comparison, we show the result of vertically averaging the A_{vox} values over the whole water column above the seafloor without any artefact masking or rectification (Fig. 15a). This generates a noisy $\bar{A}_{|vox}$ image not useful for flare detection, source localization and seepage analysis. By applying a mask (median mask; refer to Fig. 12b) that excludes the seafloor signal and seafloor-induced side-lobe distortions, strong targets in the water column like bubble streams become visible in the vertically averaged image (Fig. 15b). Shifting the water column information according to a measured bubble displacement focuses flare patterns and increases flare related signal levels compared to other distortions in the water column (Fig. 15c). By using the vertical median $(\tilde{A}_{|vox})$ rather than vertical average $(\bar{A}_{|vox})$, the resulting signal level (flare indication value) is less sensitive to spurious targets or artefacts with high signal intensities that distort only a small part of the water column (e.g., bottom signals that escaped masking). Using median averaging is therefore better suited for flare detection (Fig. 15d).

The number of vertically observable voxels ($N_{|vox}$) is used as mapping confidence value (refer to Fig. 7) to determine which points at the seafloor have been investigated well (Fig. 16a). For confident flare mapping, a minimum of 28 vertically observable voxels were required above a mapped location and for this map a -70 dB flare indication threshold was applied. For every point in the map that complied to these criteria (minimum vertically observable voxels and flare indication threshold) the arithmetic mean of the volume backscattering strength values in a layer of -20 to -30 m $\left(^{-20}_{-30}|\bar{A}_{|vox}\right)$ (refer to Fig. 8) was calculated to compare different flares/flare regions (Fig. 16b). For comparison, using only data from inside the minimum slant range (compare Fig. 12) further reduces the "observable" area for each line but the resulting map seems cleaner and less fragmented (Fig. 16c).

Mapping result from all four survey lines

The joint acoustic flare map (merged from four survey lines) of the investigated seep area is presented in Fig. 17. This map was processed using only data from inside the

Table 1. Comparison of flare intensity values of the different flares from Fig. 19. The information that was used on the final acoustic flare map has been highlighted with a gray background. Note: the mean and the integral have been computed in linear domain even though they are expressed in logarithmic domain (as dB).

Flare-LineName	Median $_{-30}^{-20}\bar{A}_{|vox}$ (dB)	Mean $_{-30}^{-20}\bar{A}_{|vox}$ (dB)	Max $_{-30}^{-20}\bar{A}_{|vox}$ (dB)	Integral over $_{-30}^{-20}\bar{A}_{|vox}$ (dB)
T-I2	−62,65	−60,25	−54,85	−44,01
T-I1	−61,77	−59,93	−55,20	−45,30
S1-I1	−70,13	−69,64	−67,91	−61,86
S1-I2	−63,4	−61,95	−59,44	−57,18
S2-I3	−66,25	−55,84	−46,78	−40,04
S2-I2	−63,23	−52,12	−40,93	−35,88
S3-I3	−66,15	−55,88	−44,96	−38,17
S3-I2	−65,46	−54,79	−44,13	−37,89
S4-I3	−67,20	−61,17	−53,74	−49,12
S4-I4	−65,11	−61,96	−57,96	−54,97
S5-I3	−63,57	−60,72	−54,43	−50,30
S5-I2	−64,80	−58,81	−54,05	−48,02
S6-I1	−63,20	−59,53	−50,95	−42,12
S6-I2	−58,21	−56,41	−52,06	−42,43
A1-I1	−64,70	−56,00	−41,78	−27,23
A1-I2	−60,50	−51,57	−38,35	−24,69
A2-I2	−65,53	−57,50	−44,84	−30,82
A2-I1	−63,26	−56,13	−43,81	−32,05
A3-I3	−63,85	−54,50	−41,31	−28,66
A3-I2	−62,49	−56,81	−45,26	−32,83
A4-I3	−58,78	−52,33	−39,87	−22,17
A4-I2	−59,93	−51,20	−37,46	−20,16

minimum slant range (see Fig. 16c) but because the line overlap was sufficient there was no difference visible on the final map when using only the median stacking method (see Fig. 16b). It shows several single flares in the east and a major seepage area in the west. To validate this result, the map was compared with flare positions that were identified manually in FMMidwater (Fig. 18). All acoustic flares detected manually were also detected with the method and thresholds applied here in a spatially very good agreement.

Comparison between different lines

We compared the relative flare intensity values $\left(_{-30}^{-20}|\bar{A}_{|vox}\right)$ of detected flares that have been covered by two neighboring survey lines to determine how consistent flare source positions and respective backscatter values are. To ensure that most flares are covered by two lines, the median masked data (see Fig. 16b) was used. The results are visualized in Fig. 19. The comparison shows positional offsets of 1–3 m between the flare maps generated from different lines. This can be related to the precision of the ship GPS system, the MBES offset calibration, but also to inaccuracies when estimating the correct bubble displacement.

Statistical properties of the flare intensity values were computed for flares depicted in Fig. 19 and are shown in

Table 2. Average alongtrack flare intensity from acoustic map vs. ROV video investigations. For every navigation point of the ROV data, the $_{-30}^{-20}\bar{A}_{|vox}$ value was looked up in the acoustic flare map and sorted to class from the corresponding video observations. Note: the Mean $\bar{A}v$ has been calculated in the linear domain, even though expressed in the logarithmic domain (dB).

Bubble activity class (from video)	Mean $_{-30}^{-20}\bar{A}_{|vox}$ (dB)	Median $_{-30}^{-20}\bar{A}_{|vox}$ (dB)
Low	−53.33	−59.85
Intermediate	−50.75	−57.31
Strong	−46.22	−53.48

Table 2. The shape of the acoustic flares on the maps is generally consistent, although flares tend to appear larger when being sampled in greater range due to the decreasing acoustic resolution. The difference between different acoustic flares is up to 21 dB. For the same flares seen in different lines, the integrated relative flare intensity shows variations of only 0.3–5.8 dB. The integrated relative flare intensity of the four flare areas A1–A4 (Fig. 19) is stronger than for the single flares S1–S6 shows similar variations of up to 4.2 dB between the different lines.
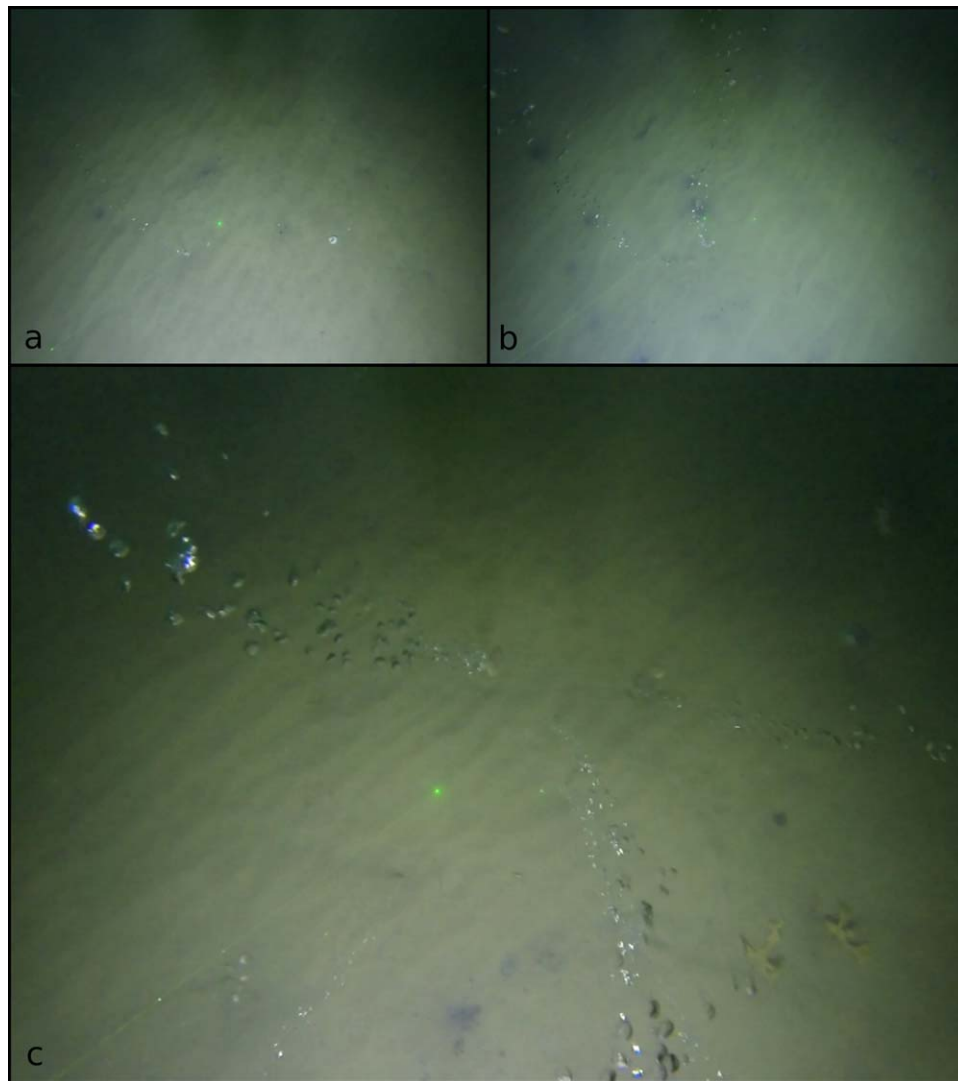
Fig. 20. ROV video observations. Examples for three bubble release classes: minor bubble release; (**b**) medium bubble release; (**c**) major bubble release.

We conclude that the acoustic flare maps are suitable to compare different flares and to determine the strongest sources in the area. In this dataset, next to the main seepage area especially the single flares S2 and S3 show strong $_{-30}^{-20}\bar{A}_{|vox}$ values and seem to be important bubble release locations. A more detailed quantitative assessment is not possible for the available dataset since short-term temporal variations of the flow rates (Greinert 2008; Schneider von Deimling et al. 2011) during the time of the survey cannot be excluded and absolute flow values for singles flares during the MBES survey time are not available.

Flare map vs. visual observations

For validating bubble release strength the main seepage area has been investigated using ROV-based videos made by downward looking cameras. The ROV survey started ca. 4 h after the MBES survey and took about 4 h to complete. The release strength was classified into four relative activity classes: no bubble activity, low bubble activity, intermediate bubble activity and strong bubble activity. A sample video for each class can be found in the Supporting Information (See also screenshots in Fig. 20a–c. To allow comparison with the acoustic flare map, the video observations were geo-referenced/positioned using the USBL-based ROV navigation data. These data were filtered, smoothed and corrected for static offsets. For each ROV position, the respective acoustic flare value from the created map was added to the respective video investigation class. To ensure a uniform standard in video quality, only data where the ROV's altitude was between 2 m and 5 m were used for the comparison.

The ROV video observations are in very good agreement with the backscatter information from the acoustic flare
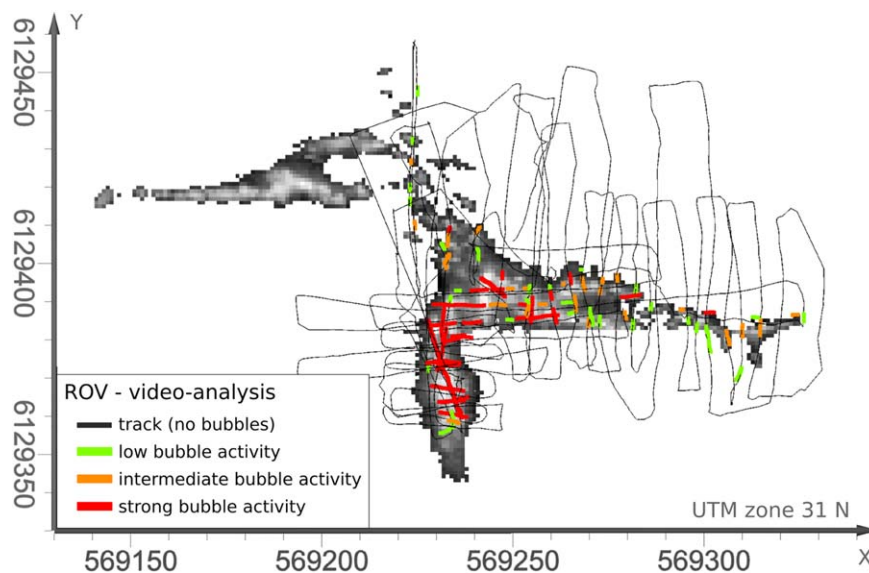
Fig. 21. ROV video analysis vs acoustic flare map.

map. This is shown in Fig. 21 and also in Table 2 where it can be seen that the along track average over the $_{-30}^{-20}\bar{A}_{|vox}$ values taken from the acoustic flare map along the ROV track increases with the bubble activity class identified from the video observations.

Discussion

The assessment shows that acoustic flare maps are efficient tools for identifying and investigating bubble sources. Backscatter information of flares can be compared at different times (in different survey lines) despite variable water currents. By inverting the current related bubble displacement shift, flares are rectified and the respective acoustic backscatter is linked to the flare source locations even if parts of the flare are not observed properly. Seafloor locations can thus be investigated for the (non-)existence of flares. Due to the beam opening angle flares do not appear as single points on a flare map. The integral of footprints from single flares is comparable enough to distinguish different bubble release activity levels. Using ROV video footage, the results of the acoustic flare mapping exercise where confirmed.

Unlike bathymetric surveys, the seafloor coverage of a flare mapping survey is not just influenced by water depth and swath opening angle but also strongly depends on water currents that shift bubble streams within the water column. In addition, distortions and unwanted targets that hide or disturb flare information reduce the area for analysis. A key point of the presented method is the clear definition of the actually observable water volume, its margins and the prediction of bubble propagation paths. We have shown two possibilities to detect the observable water mass. (1) Only using data from inside the minimum slant range. (2)

Detecting the observable water mass by calculating the median over many pings (bathymetry must be flat/homogenous and the system must be roll stabilized). The concept of the observable water mass can and should be extended in the future. Algorithms that also perform well in rough bathymetry and can dealing with non-static distortions like large fish shoals are currently been developed and implemented (see also section "Comments and recommendations" section). Known unwanted 3D targets and WCI artefacts can be excluded from the observable water volume. In deep water scenarios (>150 m) where bubbles may dissolve before they reach the sea surface, the observable water volume can be limited to the height where flares disappear. This way the actual seafloor coverage of the flare mapping WCI survey can be precisely determined even for a challenging environmental setting or distorted datasets. Areas covered insufficiently can then be re-surveyed to guarantee complete, reliable flare mapping of the seepage area.

The method presented is a step toward automated processing and analyzing of WCI data as it does no longer rely on manual identification of flares and bubble source localization. Only one template flare needs to be identified and processed to derive water currents when no other information about water currents is available (e.g., ADCP data). The method is independent of operator skills needed for manual flare identification and analyses. The flare detection is based on parameters/thresholds which are still chosen manually and are only valid for a specific combination of equipment and environment. Although they cannot be easily transferred to other setups, these values can be published, discussed and improved making this technique repeatable and reliable.

A limitation of our approach is the assumption that bubble streams adhere to a certain rise behavior. Those that

deviate from the expected model are less likely to be detected and for those "outlier flares" the strength and shape of the acoustic information projected onto the seafloor would not be quantitatively comparable. Toward this end 3D recognition techniques are seen as promising future option for searching for flares with different bubble rising behavior. This would also allow further automating flare template selection and could be supported by real-time current information from ship-mounted ADCPs.

It needs to be highlighted that surveys only provide a snapshot of the bubble release activity at the time of the survey. Short term variability in flow rates that happens during the survey (e.g., from bursting release sites) cannot be captured well and reliable results can only be derived from areas with more or less constant gas flow from distinct sources.

A next possible step toward making MBESs a precise tool for gas flow rate/flux quantifications would be acoustic in situ calibration. For this, an artificial bubble source that produces specific bubble size distributions and flow rates in a controlled and independently monitored way (visually) might be a good option. Such bubble-making system is currently developed at GEOMAR to be an additional step for quantitative bubble flow/flux studies in the future.

Comments and recommendations

Surveying in rough bathymetry

The median stacking method described only works when the artifacts in the WCI do not change in many consecutive swaths, it would fail in areas where the assumption of a homogeneous flat seafloor is not valid. In these cases defining the observable water volume by only using the data inside the minimum slant range will still exclude the strongest side-lobe artefacts caused by the seafloor; for some systems artifacts inside the minimum slant range will still remain.

When the ship's track is oriented parallel to the direction of steep bathymetric gradients (up/down slope), additional artefacts caused by the transmit side-lobes (which are directed along the ships track) may occur before the signal from the main transmit-lobe hits the seafloor and therefore inside the minimum slant range that was determined by the bottom detection. One possibility to overcome this problem is to steer the direction of the MBES main transmit-lobe perpendicular to the tilted seafloor. However, if the MBES does not allow such steering or the bathymetry is too diverse to find a simple steering angle it is best to direct the survey lines perpendicular to the steepest bathymetric gradients, parallel to depth levels.

Occurrence of large unwanted targets

Additionally to noise and artefacts, water column echos can also be disturbed by other undesired targets (not bubble stream related) which can hide or falsify bubble stream related acoustic information. Vertically averaging over the

rectified observable water mass is effective in limiting disturbances by targets which are much smaller than the acoustic flares. Still, large targets like massive fish shoals can interfere with the bubble stream detection. To avoid detection of virtual (false) acoustic flares, these targets must be identified and defined as sub volumes which can be excluded from the observable water mass similarly to side-lobe distortions. In case such targets occur, manual editing in combination with our automated approach is recommended. Using a 3D editor detected false targets can be manually marked as "masked targets."

Multibeam swath mode (single/dual swath)

Many MBES including the EM302 offer the possibility to emit two swaths per ping cycle (primary and secondary) to double the swath density (named multi-ping or dual swath mode). During the assessment the dual-swath mode was deactivated. While the increase in swath density is generally desirable, the second swath usually shows different and more artefacts than the first one. Simply stacking multiple images would therefore lead to a blurred image which is ineffective for detecting and masking static noise. It is recommended to distinguish between the primary and secondary swath and create two different stacked images and masks for either the primary or secondary swath. Depending on the data it might be possible to merge both swath data sets for further analyses or process both swath data sets separately and merge/compare the final result in their map representation (e.g., flare position, signal strength).

References

Artemov, Y. G. 2006. Software support for investigation of natural methane seeps by hydroacoustic method. Mar. Ecol. J. **5**: 57–71.

Artemov, Y. G., V. N. Egorov, G. G. Polikarpov, and S. B. Gulin. 2007. Methane emission to the hydro-and atmosphere by gas bubble streams in the Dnieper paleo-delta, the Black Sea. Rep. Natl. Acad. Sci. Ukraine **5**: 110–116.

Brussaard, C. 2013. CRUISE REPORT 64PE376 NIOZ Monitoring Leg 1. Royal Netherlands Institute for Sea Research (NIOZ).

Clarke, J. E. H. 2006. Applications of multibeam water column imaging for hydrographic survey. Hydrogr. J. **120**: 3–15.

Clift, R., J. R. Grace, and M. E. Weber. 1978. Bubbles, drops, and particles. Academic Press.

Colbo, K., T. Ross, C. Brown, and T. Weber. 2014. A review of oceanographic applications of water column data from multibeam echosounders. Estuar. Coast. Shelf Sci. **145**: 41–56. doi:10.1016/j.ecss.2014.04.002

Dupré, S., L. Berger, N. Le Bouffant, C. Scalabrin, and J. F. Bourillet. 2014. Fluid emissions at the Aquitaine Shelf (Bay of Biscay, France): A biogenic origin or the

expression of hydrocarbon leakage? Cont. Shelf Res. **88**: 24–33. doi:10.1016/j.csr.2014.07.004

Dupré, S., and others. 2015. Tectonic and sedimentary controls on widespread gas emissions in the Sea of Marmara: Results from systematic, shipborne multibeam echo sounder water column imaging. J. Geophys. Res. Solid Earth **120**: 2014JB011617. doi:10.1002/2014JB011617

Fisher, R. E., and others. 2011. Arctic methane sources: Isotopic evidence for atmospheric inputs. Geophys. Res. Lett. **38**: L21803. doi:10.1029/2011GL049319

FMMidwater. 2014. Fledermaus. QPS Canada Inc.

Foote, K. G., D. Chu, T. R. Hammar, K. C. Baldwin, L. A. Mayer, L. C. Hufnagle, and J. M. Jech. 2005. Protocols for calibrating multibeam sonar. J. Acoust. Soc. Am. **117**: 2013–2027. doi:10.1121/1.1869073

Gardner, J. V., M. Malik, and S. Walker. 2009. Plume 1400 meters high discovered at the seafloor off the Northern California Margin. Eos Trans. AGU **90**: 275–275. doi:10.1029/2009EO320003

Gentz, T., E. Damm, J. Schneider von Deimling, S. Mau, D. F. McGinnis, and M. Schlüter. 2014. A water column study of methane around gas flares located at the West Spitsbergen continental margin. Cont. Shelf Res. **72**: 107–118. doi:10.1016/j.csr.2013.07.013

Greinert, J. 2008. Monitoring temporal variability of bubble release at seeps: The hydroacoustic swath system GasQuant. J. Geophys. Res. **113**: C07048. doi:10.1029/2007JC004704

Greinert, J., and B. Nützel. 2004. Hydroacoustic experiments to establish a method for the determination of methane bubble fluxes at cold seeps. Geo Mar. Lett. **24**: 75–85. doi:10.1007/s00367-003-0165-7

Greinert, J., Y. Artemov, V. Egorov, M. Debatist, and D. Mcginnis. 2006. 1300-m-high rising bubbles from mud volcanoes at 2080m in the Black Sea: Hydroacoustic characteristics and temporal variability. Earth Planet Sci. Lett. **244**: 1–15. doi:10.1016/j.epsl.2006.02.011

Greinert, J., D. F. McGinnis, L. Naudts, P. Linke, and M. De Batist. 2010. Atmospheric methane flux from bubbling seeps: Spatially extrapolated quantification from a Black Sea shelf area. J. Geophys. Res. **115**: C01002. doi:10.1029/2009JC005381

Gurshin, C. W. D., J. M. Jech, W. H. Howell, T. C. Weber, and L. A. Mayer. 2009. Measurements of acoustic backscatter and density of captive Atlantic cod with synchronized 300-kHz multibeam and 120-kHz split-beam echosounders. ICES J. Mar. Sci. **66**: 1303–1309. doi:10.1093/icesjms/fsp052

Hampel, F. R. 1971. A general qualitative definition of robustness. Ann. Math. Stat. **42**: 1887–1896. doi:10.1214/aoms/1177693054

Hornafius, J. S., D. Quigley, and B. P. Luyendyk. 1999. The world's most spectacular marine hydrocarbon seeps (Coal Oil Point, Santa Barbara Channel, California): Quantification of emissions. J. Geophys. Res. **104**: 20703–20711. doi:10.1029/1999JC900148

IVS 3D, Inc. 2012. Generic water column format version 2.3 [WWW Document] [accessed 2015 Jan 19] Available from https://confluence.qps.nl/display/KBE/Generic+Water+Column+Format

Leblond, I., C. Scalabrin, and L. Berger. 2014. Acoustic monitoring of gas emissions from the seafloor. Part I: Quantifying the volumetric flow of bubbles. Mar. Geophys. Res. **35**: 191–210. doi:10.1007/s11001-014-9223-y

Leifer, I., B. P. Luyendyk, J. Boles, and J. F. Clark. 2006. Natural marine seepage blowout: Contribution to atmospheric methane. Global Biogeochem. Cycles **20**: GB3008. doi:10.1029/2005GB002668

Leifer, I., and D. Culling. 2010. Formation of seep bubble plumes in the Coal Oil Point seep field. Geo-Mar. Lett. **30**: 339–353. doi:10.1007/s00367-010-0187-x

Lurton, X. 2010. An introduction to underwater acoustics: Principles and applications, 2nd ed. Springer-Praxis books in geophysical sciences. Springer.

MacDonald, I. R., I. Leifer, R. Sassen, P. Stine, R. Mitchell, and N. Guinasso. 2002. Transfer of hydrocarbons from natural seeps to the water column and atmosphere. Geofluids **2**: 95–107. doi:10.1046/j.1468-8123.2002.00023.x

Mau, S., and others. 2015. Seasonal methane accumulation and release from a gas emission site in the central North Sea. Biogeosciences **12**: 5261–5276. doi:10.5194/bg-12-5261-2015

Medwin, H. 1998. Fundamentals of acoustical oceanography, Applications of modern acoustics. Academic Press.

Muyakshin, S. I., and E. Sauter. 2010. The hydroacoustic method for the quantification of the gas flux from a submersed bubble plume. Oceanology **50**: 995–1001. doi:10.1134/S0001437010060202

Nikolovska, A., H. Sahling, and G. Bohrmann. 2008. Hydroacoustic methodology for detection, localization, and quantification of gas bubbles rising from the seafloor at gas seeps from the eastern Black Sea. Geochem. Geophys. Geosyst. **9**: Q10010. doi:10.1029/2008GC002118

Ostrovsky, I., D. F. McGinnis, L. Lapidus, and W. Eckert. 2008. Quantifying gas ebullition with echosounder: The role of methane transport by bubbles in a medium-sized lake. Limnol. Oceanogr.: Methods **6**: 105–118. doi:10.4319/lom.2008.6.105

Ostrovsky, I., and J. Tęgowski. 2010. Hydroacoustic analysis of spatial and temporal variability of bottom sediment characteristics in Lake Kinneret in relation to water level fluctuation. Geo-Mar. Lett. **30**: 261–269. doi:10.1007/s00367-009-0180-4

Perrot, Y., P. Brehmer, G. Roudaut, P. Gerstoft, and E. Josse. 2014. Efficient multibeam sonar calibration and performance evaluation. Int. J. Eng. Sci. Innov. Technol. **3**: 808–820.

Rahman Talukder, A., and others. 2013. Natural hydrocarbon seepage on the continental slope to the east of Mississippi Canyon in the northern Gulf of Mexico. Geochem. Geophys. Geosyst. **14**: 1940–1956. doi:10.1002/ggge.20130

Römer, M., H. Sahling, T. Pape, G. Bohrmann, and V. Spieß. 2012. Quantification of gas bubble emissions from

submarine hydrocarbon seeps at the Makran continental margin (offshore Pakistan). J. Geophys. Res. **117**: C10015. doi:10.1029/2011JC007424

Sahling, H., and others. 2009. Vodyanitskii mud volcano, Sorokin trough, Black Sea: Geological characterization and quantification of gas bubble streams. Mar. Pet. Geol. **26**: 1799–1811. doi:10.1016/j.marpetgeo.2009.01.010

Sahling, H., and others. 2014. Gas emissions at the continental margin west of Svalbard: Mapping, sampling, and quantification. Biogeosciences **11**: 6029–6046. doi:10.5194/bg-11-6029-2014

Schneider von Deimling, J., J. Brockhoff, and J. Greinert. 2007. Flare imaging with multibeam systems: Data processing for bubble detection at seeps: FLARE IMAGING. Geochem. Geophys. Geosyst. **8**: Q06004. doi:10.1029/2007GC001577

Schneider von Deimling, J., J. Greinert, N. R. Chapman, W. Rabbel, and P. Linke. 2010. Acoustic imaging of natural gas seepage in the North Sea: Sensing bubbles controlled by variable currents. Limnol. Oceanogr.: Methods **8**: 155. doi:10.4319/lom.2010.8.155

Schneider von Deimling, J., G. Rehder, J. Greinert, D. F. McGinnnis, A. Boetius, and P. Linke. 2011. Quantification of seep-related methane gas emissions at Tommeliten, North Sea. Cont. Shelf Res. **31**: 867–878. doi:10.1016/j.csr.2011.02.012

Schneider von Deimling, J., and C. Papenberg. 2012. Technical note: Detection of gas bubble leakage via correlation of water column multibeam images. Ocean Sci. **8**: 175–181. doi:10.5194/os-8-175-2012

Schneider von Deimling, J., P. Linke, M. Schmidt, and G. Rehder. 2015. Ongoing methane discharge at well site 22/4b (North Sea) and discovery of a spiral vortex bubble plume motion. Mar. Pet. Geol. **68**: 718–730. doi:10.1016/j.marpetgeo.2015.07.026

Schroot, B. M., G. T. Klaver, and R. T. E. Schüttenhelm. 2005. Surface and subsurface expressions of gas seepage to the seabed—examples from the Southern North Sea. Mar. Pet. Geol. **22**: 499–515. doi:10.1016/j.marpetgeo.2004.08.007

Smith, A. J., J. Mienert, S. Bünz, and J. Greinert. 2014. Thermogenic methane injection via bubble transport into the upper Arctic Ocean from the hydrate-charged Vestnesa Ridge, Svalbard. Geochem. Geophys. Geosyst. **15**: 1945–1959. doi:10.1002/2013GC005179

Solomon, E. A., M. Kastner, I. R. MacDonald, and I. Leifer. 2009. Considerable methane fluxes to the atmosphere from hydrocarbon seeps in the Gulf of Mexico. Nat. Geosci. **2**: 561–565. doi:10.1038/ngeo574

Urick, R. J. 1996. Principles of underwater sound, 3rd ed. Peninsula Publ.

Veloso, M., J. Greinert, J. Mienert, and M. De Batist. 2015. A new methodology for quantifying bubble flow rates in deep water using splitbeam echosounders: Examples from the Arctic offshore NW-Svalbard. Limnol. Oceanogr.: Methods **13**: 267–287. doi:10.1002/lom3.10024

Weber, T. C., L. A. Mayer, J. Beaudoin, K. Jerram, M. A. Malik, B. Shedd, and G. A. Rice. 2012. Mapping gas seeps with the deepwater multibeam echosounder on Okeanos explorer. Oceanography **25**: 54–55.

Westbrook, G. K., and others. 2009. Escape of methane gas from the seabed along the West Spitsbergen continental margin. Geophys. Res. Lett. **36**: L15608. doi:10.1029/2009GL039191

Conflict of Interest

None declared.